

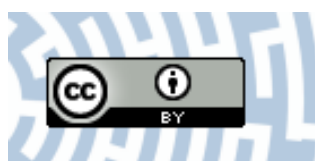


You have downloaded a document from  
**RE-BUŚ**  
repository of the University of Silesia in Katowice

**Title:** The finite element method in tribological studies of polymer materials in tribo-pair with oxide layer

**Author:** Marek Kubica, Władysław Skoneczny

**Citation style:** Kubica Marek, Skoneczny Władysław. (2013). The finite element method in tribological studies of polymer materials in tribo-pair with oxide layer. "Tribology Letters" (Vol. 52, iss. 3 (2013), s. 381-393), doi 10.1007/s11249-013-0222-y



Uznanie autorstwa - Licencja ta pozwala na kopiowanie, zmienianie, rozprowadzanie, przedstawianie i wykonywanie utworu jedynie pod warunkiem oznaczenia autorstwa.



# The Finite Element Method in Tribological Studies of Polymer Materials in Tribo-Pair with the Oxide Layer

Marek Kubica · Władysław Skoneczny

Received: 11 June 2013 / Accepted: 16 September 2013 / Published online: 13 October 2013  
© The Author(s) 2013. This article is published with open access at Springerlink.com

**Abstract** We present an approach to the analysis of mechanisms of the tribological contact of a thin  $\text{Al}_2\text{O}_3$  oxide layer formed under hard anodizing conditions on a plate made of the aluminium alloy EN AW-5251. The oxidation of the 50- $\mu\text{m}$  ceramic layer was carried out for 60 min in a three-component electrolyte (SAS), a three-component electrolyte consisting of adipic, sulphuric and oxalic acid, at a temperature of 298.15 K and a current density of 3  $\text{A}/\text{dm}^2$ . A three-dimensional oxide coating model, based on the computer analysis of images from a scanning electron microscope, is proposed. Tribological tests of stresses, strains and dislocations formed in the oxide layer and in the sample material (a block) were conducted. Modified polytetrafluoroethylene (TG15, TKG20/5, TMP12) and polyetheretherketone with carbon fibre and graphite were used as samples for tests in the tribological couple rider-plate of a linear reciprocating friction tester. A tribological couple modelled in the Solid Edge CAD programme was subjected to numerical analyses using the finite element method in the Autodesk Simulation Multiphysics programme under conditions consistent with actual conditions for contact pressures of 0.25, 0.50, and 1.0 MPa.

**Keywords** Solid lubrication film thickness · Coatings · Friction-reducing · PTFE · Aluminium alloy

## 1 Introduction

One of the most important phenomena accompanying friction is the surface wear of the materials involved. Tribology seeks to limit the effects of the destructive friction force, i.e., to reduce the energy dissipated as the surface wear of interacting components. Surface films formed on moving components play an important role in the efforts to achieve this goal. When properly formed and used, a tribological surface film allows significant reduction of the friction coefficient and thus the prolongation of the operational durability of tools as well as machine and device parts [1]. Coatings are used to obtain tribological materials in order to improve operational properties and to provide suitable decorative properties. Most of the coatings created for tribological applications are thin and hard anti-wear coatings. Most of the alloys in wide use in the automotive, aircraft, and food industries are primarily aluminum ones. These are characterized by a low density, relatively high-strength properties, resistance to atmospheric corrosion and very good plastic properties, all of which are beneficial from the technological point of view. The main drawback of aluminum alloys is their low resistance to friction wear. Many studies have therefore focused on eliminating this drawback, for example, by applying various surface engineering methods. The anodic oxidation process, which leads to the formation of the upper layer of aluminium (phase  $\alpha\text{-Al}_2\text{O}_3$ ) and subsequently to increased hardness and improved tribological properties [2], is a commonly used method for improving the mechanical properties of these alloys.

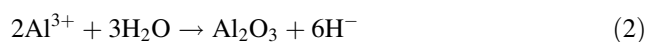
Ceramic materials have oxide layers, and these layers will probably be incorporated into the upcoming generation of construction materials. These materials have suitable physicochemical properties that make them ideally suitable

M. Kubica (✉) · W. Skoneczny  
Faculty of Computer Science and Materials Science, University of Silesia, 12, Bankowa, 40-007 Katowice, Poland  
e-mail: mkubica@us.edu.pl

W. Skoneczny  
e-mail: wladyslaw.skoneczny@us.edu.pl

for a vast range of applications in structures working at high temperatures (such as combustion engines, gas turbines and multi-piston compressors). Aluminium oxide  $\text{Al}_2\text{O}_3$  may also be used in the production of machining tools blades and in integrated circuits of electrical engineering systems, as well as in fibre optics and biomedical engineering. An analysis of market trends leads to the conclusion that ceramic materials and composites are strong candidates for becoming the most common materials for future applications in the automotive industry. Ceramic materials are light and resistant to heat, high-temperature creep, corrosion, erosion and wear. The layer created by hard anodizing shows higher mechanical properties than the aluminium alloy as well as a high adhesion, and it can be used in lubricant free sliding matching that can simulate the operation of pneumatic servo-motors. In this case, it has a lower friction coefficient and higher wear resistance than the pure aluminium alloy and is a better material for these applications [3–6].

In the Division of Surface Layer Technologies, University of Silesia, the layers are obtained using the electrochemical method. Anodic production of the oxide coating ( $\text{Al}_2\text{O}_3$ ) on aluminium is by the hard anodizing process, and its alloys are produced using the electrolytic method where the micro-hardness of the coating is at least 5,000 MPa and its thickness is not less than 25  $\mu\text{m}$  [7]. In the initial phase of the passage of current in the Al (anode)–electrolyte–cathode system, a thin compact  $\text{Al}_2\text{O}_3$  layer (the so-called a barrier layer) is formed, which then transforms into a porous layer. The barrier layer is formed as a result of the migration of  $\text{Al}^{3+}$  ions in the electric field and their subsequent reactions with  $\text{O}^{2-}$  or  $\text{OH}^-$  ions and/or the formation of anhydrous  $\text{Al}_2\text{O}_3$ . Basic chemical reactions which take place during the process of  $\text{Al}_2\text{O}_3$  layer formation via anodizing may be expressed as follows [8]:



The formation of the barrier layer causes an increase in electrical resistance. As the volume of the oxide being formed is greater than the volume of metal, tensile stresses are created inside the oxide layer that lead to cracks in the barrier layer. This is the main factor contributing to the formation of nonporous nanofibres through which the penetration of the electrolyte from the external side of the formed layer takes place. The electrolyte can penetrate the nonporous layer, which leads to the formation of hydrated aluminium oxide, an electrically insulating colloid. Two processes take place at the bottom of the nonporous nanofibres: the formation of an oxide layer and the opening

of the latter by the electrolyte. The layer thus formed has good mechanical and adhesive properties and can be used in non-lubricated sliding. The structure of the ceramic  $\text{Al}_2\text{O}_3$  layers is one of the main factors determining the chemical, physical, surface and mechanical properties. The resistance to wear of the polymer–oxide coating layer depends on porosity, morphology and roughness of the ceramic layer surface. The analysis of microscopic images and physicochemical properties of  $\text{Al}_2\text{O}_3$  coatings has led to the creation of various theories on the structure and formation mechanism of the oxide layer, including those of Csokan [9], Keller et al. (KHR) [10–12], Sulka [13, 14] and Skoneczny [15]. The model proposed by Skoneczny [15] of the actual structure of the oxide coating layer obtained in a three-component SAS electrolyte,  $\text{H}_2\text{SO}_4$ ,  $(\text{CH}_2)_4(\text{COOH})_2$ , at temperatures ranging from 293 to 313 K and current densities of 2 to 4  $\text{A}/\text{dm}^2$  consists of a thin barrier layer directly adjoining the metal layer and a porous upper layer. Micropores formed as a result of aluminium oxide nanofibres contacting one another due to the formation of the columnar structure of a pore have an equilateral triangle shape where the sides have been replaced by an arc formed from a circular section. Energy interferences in the oxide layer and the local etching of grain boundaries of the substrate material and admixtures caused the formation of macropores [15].

## 2 Experimental Setup

In this section we discuss the creation of oxide layers by means of hard anodizing. Studies of the nanostructure of the  $\text{Al}_2\text{O}_3$  coating, based on the images from a scanning microscope, are presented.

### 2.1 Obtaining $\text{Al}_2\text{O}_3$ Layers by Means of Hard Anodizing

Anodic oxide coatings (AOC) are obtained from electrolytes with an average re-solution capacity [16–18]. The oxidation of the ceramic layer was carried out for 60 min in a three-component SAS electrolyte at a temperature of 298.15 K and a current density of 3  $\text{A}/\text{dm}^2$ . Adipic acid  $[(\text{CH}_2)_4(\text{COOH})_2]$  was selected due to the possibility of attaining with it the balance between blocking and stopping processes via adsorption of the  $[\text{OOH}-(\text{CH}_2)_4-\text{COO}]^{2-}$  compound onto the surface of the EN AW-5251 aluminium alloy during electrolytic treatment. It was added to the system via the electrolyte mixture of sulphurous and oxalic acid. Thanks to this solution the best mechanical properties were obtained, compared with other dicarboxylic acids [19]. The nanostructure of the surface is one of the most important characteristics of the  $\text{Al}_2\text{O}_3$ , which to a large degree affects its tribological performance in unlubricated

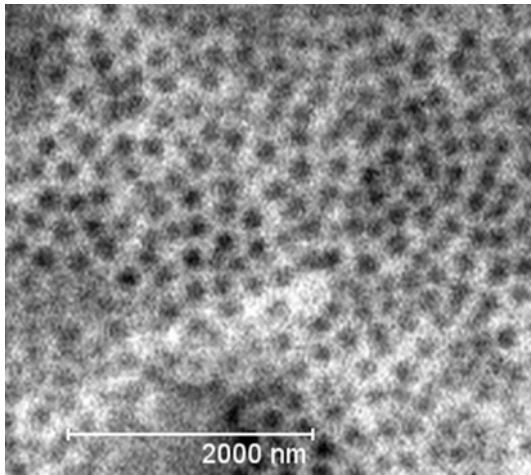
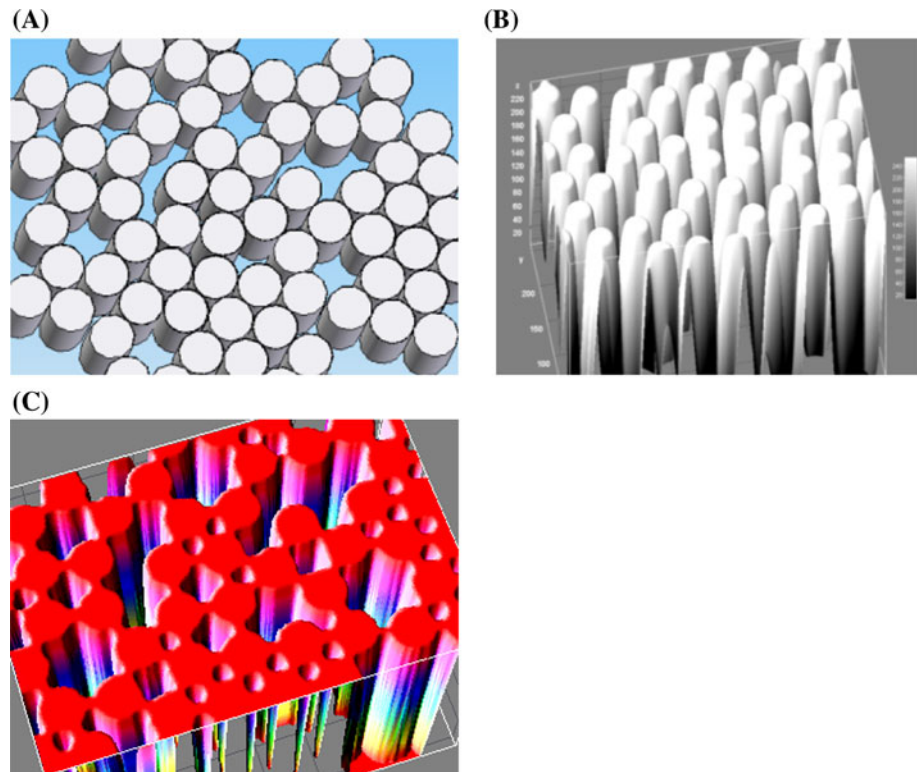


**Fig. 1** Scanning electron microscope (SEM) images of nanostructure nanoarrows of aluminium oxide ( $\text{Al}_2\text{O}_3$ ) created in the SAS electrolyte

sliding contacts. The image of the surface morphology was derived from images observed with a scanning electron microscope of the  $\text{Al}_2\text{O}_3$  layer with visible nonporous nanofibres and was obtained in the hard anodizing process in a three-component SAS electrolyte at a temperature of 298.15 K, a current density of 3 A/dm<sup>2</sup> and an oxidation time of 60 min (Fig. 1).

**Fig. 2** Virtual models of the plane of the oxide layer: **a** Solid Edge, **b**, **c** ImageJ



## 2.2 Examination of the Nanostructure of the $\text{Al}_2\text{O}_3$ Coating

The size and shape of the nonporous nanofibres depend on the substrate metal structure, the type of electrolyte as well as the conditions in which the anodizing process is conducted. Nanopores which are the result of aluminium oxide nanofibres contacting one another as well as of their arrangement and growth are formed in a perfect columnar structure without energy interference. A cross-section of a pore has in that case an equilateral triangle shape whose sides have been covered by an arc formed from a fibre section. Structures for nanofibres creating micropores that have been formed as a result of the transformation of energy interferences in the substrate structure into the oxide coating may assume the shape of a rhombus, pentagon or hexagon [20].

The appearance of a structure obtained from the combination of various nonporous layers was proposed as the Solid Edge and ImageJ model (Fig. 2).

A computer analysis of the binary image conducted using the ImageJ programme showed that the average surface of a pore is 5,140 nm<sup>2</sup> and the porosity = 4.86. Average surface areas of nonporous nanofibres are as follows: triangle-shaped, 1,003 nm<sup>2</sup>; rhombus-shaped, 5,169 nm<sup>2</sup>; pentagon-shaped, 13,656 nm<sup>2</sup>; hexagon-shaped, 26,696 nm<sup>2</sup>. The largest nanopore has a surface area of 3,640 nm<sup>2</sup>.

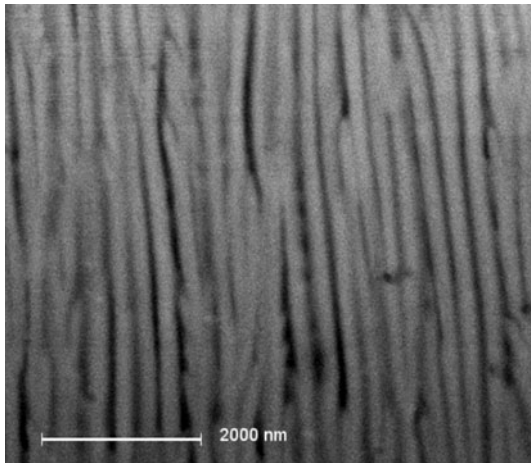


**Fig. 3** SEM image of the oxide layer created in the SAS electrolyte

Based on images of a properly prepared microsection (Fig. 3) of a lateral layer of an oxidized sample, it was possible to establish the appearance, arrangement and thickness of the aluminium oxide nanofibres. Calculations of the thickness of the nanofibres (Fig. 4) were carried out on the binary image of an aluminium oxide layer using a computer image analysis (CIA) conducted in the ImageJ programme. The measurements indicate that the average nanofibre thickness is 156 nm. Measurements 1–10 were conducted in the lower parts of the image, 11–20 in the middle and 21–30 in the upper parts. The diagram shows the growing trend of changes in nanofibre thickness.

### 2.3 Finite Element Modelling

Computer technology allows the use of software to perform analyses and to simulate real models and objects while taking into account the properties of materials and tribological interaction conditions. For the purpose of solving the examined rider-plate system, we used the finite element method (FEM) to make calculations. This method is currently the most commonly used by programmes supporting computer design and manufacturing. Its most important feature is the division of the examined continuous system

into an equivalent system of smaller bodies and finite elements which are connected with each other at common points called nodes; it is at the nodes where calculations are made. Programmes supporting numerical calculations to estimate strength use the Huber–Mises–Hencky hypothesis according to which material is transformed into a plastic state when the energy density of non-dilatational strains reaches a certain threshold value characteristic of the material [21].

We used a computer aided engineering (CAE) software, Autodesk Multiphysics Simulation (previously Algor; Autodesk Inc., San Rafael, CA), to perform the FEM calculations. The application allows for calculating stress, and various analytical techniques are available to assist in determining the suitability of model. Derived quantities include von Mises and Tresca criteria, maximum and minimum principal stresses and element-specific output. Since the accuracy of the analytical results depends on the construction of the mesh and the application of FEM parameters, the results environment provides a precision estimate at shared nodes. The software uses the stress-to-nodes method for calculating stress estimations. The equation used is von Mises:

$$\sqrt{0.5[(S_x - S_y)^2 + (S_y - S_z)^2 + (S_z - S_x)^2] + 3(S_{xy}^2 + S_{yz}^2 + S_{zx}^2)} \tag{4}$$

where  $S_x$ ,  $S_y$  and  $S_z$  are the axial stresses in the global directions, and  $S_{xy}$ ,  $S_{yz}$ , and  $S_{zx}$  are the shear stresses. In terms of the principal stresses  $S_1$ ,  $S_2$  and  $S_3$ :

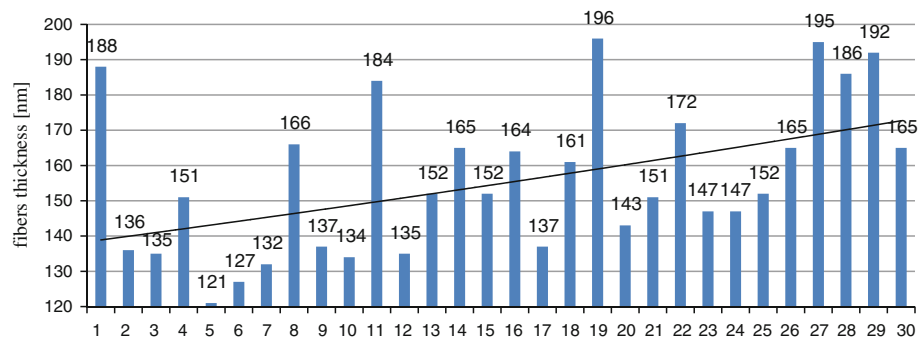
$$\sqrt{0.5[(S_1 - S_2)^2 + (S_2 - S_3)^2 + (S_3 - S_1)^2]} \tag{5}$$

For the maximum stress and maximum strain criteria, various factors of safety have to be considered. First, the factors of safety based on the top and bottom surface of the laminae maximum stress are:

$$\frac{X_c}{|\sigma_1|}, \frac{X_t}{|\sigma_1|}, \frac{Y_c}{|\sigma_2|}, \frac{Y_t}{|\sigma_2|}, \frac{S}{|\tau_{12}|} \tag{6}$$

where  $\sigma$  is the calculated normal stress in direction 1 or 2,  $X$  and  $Y$  are the allowable stresses in direction 1 and 2

**Fig. 4** Some of the results for the measurement of the thickness of aluminium oxide nanofibres



(compression or tension matched to the calculated stress),  $\tau_{12}$  is the calculated shear stress and  $S$  is the allowable shear stress. The factors of safety for the maximum strain are:

$$\frac{T_{1c}}{|\varepsilon_1|}, \frac{T_{1t}}{\varepsilon_1}, \frac{T_{2c}}{|\varepsilon_2|}, \frac{T_{2t}}{\varepsilon_2}, \frac{S}{|\gamma_{12}|} \quad (7)$$

where  $\varepsilon$  is the calculated normal strains in direction 1 or 2,  $T$  is the appropriate allowable strains in direction 1 and 2 (compression or tension matched to the calculated strains),  $\gamma_{12}$  is the calculated shear strains and  $S$  is the allowable shear strains. The results displayed are then the Tsai–Wu failure criterion. first consider the value  $F$ :

$$F = F_1\sigma_1 + F_2\sigma_2 + F_{11}\sigma_1^2 + 2F_{12}\sigma_1\sigma_2 + F_{22}\sigma_2^2 + F_{66}\tau_{12}^2 \quad (8)$$

where

$$F_1 = \left(\frac{1}{X_t}\right) - \left(\frac{1}{X_c}\right), F_2 = \left(\frac{1}{Y_t}\right) - \left(\frac{1}{Y_c}\right), \\ F_{11} = \frac{1}{(X_t \cdot X_c)}, F_{22} = \frac{1}{(Y_c \cdot Y_t)}, F_{66} = \frac{1}{(S \cdot S)} \quad (9)$$

$\sigma$  and  $\tau$  are calculated normal and shear stresses, respectively, and all other values are material inputs. Most of the formulas for the stress results described previously can be used to display the strain results in a model. Strain energy density is such that the model will be shaded according to the strain energy density. The strain energy of an element is defined as the energy absorbed by the element due to the loading. This can be calculated on a per volume basis as:

$$u = \frac{\sigma^2}{2E} \quad (10)$$

It is possible to calculate displacement in the programme. The commands available are as follows:

- Magnitude sets the display to be based on the magnitude of the displacement. This will always be a positive value. The magnitude is the total distance the node has move.  $\text{Mag} = \sqrt{(d_x)^2 + (d_y)^2 + (d_z)^2}$  where  $X, Y$  and  $Z$  are directions.
- Vector plot sets the display to be based on the magnitude of the displacement, showing the result as a vector (arrow) drawn at each node [22].

Tribological contact with two loaded surfaces in relative motion is a complex system which is not easy to understand or simulate. The system is even more complicated when special coatings like  $\text{Al}_2\text{O}_3$  are introduced onto the plate surface. Many studies have been carried out at macro-, micro- and even nanolevels [3–5]. The material properties are the most important factor contributing to tribological

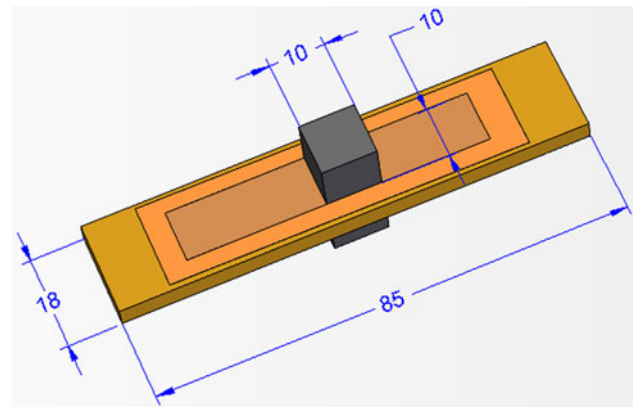


**Fig. 5** Dimensions of the sample, and counter-sample in the rider-plate system

performance. The most important properties in the computer programmes that use FEM as a method of calculation are: density, Young's modulus, Poisson ratio, shear strength and module of elasticity [23–26]. Hardness is defined as the material resistance to permanent strains induced by focused forces which affect small surfaces [27, 28].

#### 2.4 Configuration of the Rider-Plate Friction Couple in Reciprocating Motion

The scratch test configuration was a sample (rider) of 10, 10 and 10 mm<sup>3</sup> (length, width, thickness) made of different materials and a counterface (plate) of 85, 18 and 4 mm<sup>3</sup> (Fig. 5) made of EN AW-5251 with an  $\text{Al}_2\text{O}_3$  oxide layer. The counterface material was chosen primarily because of its high susceptibility to oxidation.

To ensure an increase in the service life of kinematic couples in lubricant-free machines, sliding partners, i.e. a polymer (or its modifications) and an anodic hard coating, are applied onto the aluminium alloys. Tribological properties of the  $\text{Al}_2\text{O}_3$  layer on EN AW-5251 can be controlled by changing the conditions of the hard anodizing process, namely, the composition, pH, electrolyte temperature, process time and anodic current density [29]. A change in any of these process parameters allows the morphology and roughness of the surface and thickness and micro hardness of oxide layer to be modified, which has a significant impact on their resistance to wear and, consequently, on the operational durability of the tribological couple [30].

#### 2.5 Sample Materials Used in the Tribological Test

Practically all polymers can be used as matrices to obtain polymer composites, although polytetrafluoroethylene (PTFE) and its modifications are the most attractive in this respect due to their perfect friction properties and chemical

inertness. An analysis of the literature shows that PTFE with carbon fibre and graphite (PEEK/BG) is an equally good material for tribological tests on interactions with the  $\text{Al}_2\text{O}_3$  layer [31]. The tribological tests were conducted for a lubricant free sliding couple: PEEK/BG, the anodic hard coating, on a tribological stand, RS2007, in reciprocating motion, under conditions corresponding to the service conditions of lubricant-free servomotors. An effect of the interaction between PEEK/BG and anodic hard coatings was the deposition of a polymer sliding film onto the surfaces of all  $\text{Al}_2\text{O}_3$  counter-specimens [19]. Various authors [32–35] have shown that oxide layer obtained in an acid electrolyte  $(\text{COOH})_2$  on an EN AW-5251 aluminium alloy substrate has very good properties when coupled with the TG15 material. Published reports suggest that in the case of tribological tests of lubricant-free couples it is also worthwhile to take a look at the PTFE material, especially its modifications, from which one can obtain materials such as TG15, TGK20/5 and TMP12 [36].

The PTFE produced by the nitrogen plants of Tarnów and Mościce S.A. (Tarnów, Poland) has an outstanding thermal stability, good solvent resistance and a low friction coefficient. PTFE has been widely used as an engineering plastic. It is chemically inert and characterized by a low friction coefficient (the lowest among all technical materials), which provides it with very good sliding properties. It also has very low adhesion and therefore the lowest friction coefficients for almost all solid bodies. These parameters make it a great matrix for obtaining polymer composites [37].

High-performance polymers are used for many industrial applications because of their excellent mechanical properties that are preserved also at high temperatures. PTFE is the most attractive of the high-performance polymers. PEEK is often used as a composites matrix. PTFE and graphite enhance the tribological behaviour of the molded part, whereas the carbon fibres are responsible for the high mechanical performances. Commercial bushes were acquired from a manufacturer who started to produce the component depicted in several high-performance polymers. This bush was designed for small-sized electric motors instead of a traditional brass because of the low weight and production time. The PEEK 450 FC 30 (Victrex, Greenville, SC) was adapted to the injection mold with 10 % carbon fibre, 10 % graphite and 10 % PTFE [38–42].

## 2.6 Characteristics of the Tribological Test

The tribological test was conducted under technically dry friction conditions on the RS2007 tester. The test stand comprises the following units: engine, gear-motor, inverter, clutch, guides and connecting rod. Friction forces and the number of cycles (friction distance) are measured during

stand tests. Technical parameters of the tester include the plane reciprocating motion (Fig. 6a), plane–plane contact speed from 0 to 5 m/s and load from 5 to 100 N (Fig. 6b).

In the tests that were conducted, the unit pressure on a sample amounted to 0.25, 0.5, and 1 MPa at the average sliding speed of 1 m/s for all samples. A sliding rider-plate couple was modelled using the Solid Edge environment (CAD-type software) for sizes compatible with actual ones [20].

The three-dimensional model obtained was exported to the Autodesk Simulation Multiphysics environment supporting engineering calculations where a strength analysis under conditions corresponding to real ones was conducted. Appropriate properties of materials which are decisive while conducting a FEM analysis were entered into the programme (Table 1). Material properties of the layer were specified as anisotropic. After the task material properties, the mesh-on model was constructed.

## 2.7 Finite Element Mesh

The number of nodes in the tested model was 36,171, the number of elements was 48,283 of which 11,396 were layer elements, 27,626 were plate elements and 9,261 were rider elements. The types of elements were bricks (8 nodes)—82.85 % (volume); pyramids (5 nodes)—6.77 %; tetrahedra (4 nodes)—5.86; wedges (6 nodes)—4.52 %. Before the launch of the analysis we performed a check on the model in Simulation Multiphysics and confirmed that the FEM model is as intended. The programme verified that there are no holes, no missing boundary conditions, etc. The geometry decoder tested that all of the lines in the model are connected in such a way that valid elements can be formed out of those lines. No lines were present in the model that cannot be used to form legitimate elements or other decoding problems. The program checked if the material properties are appropriate after checking the geometry-performed simulations for variable boundary conditions.

## 3 Experimental Results

The FEM analyses provided an answer in the form of distributions of stresses, strains and dislocations formed as a result of the applied loads and motion for various sample materials. The distribution of stresses was found to be very similar regardless of the type of material used, while the values of stresses and strains in specific local regions changed. Figures 9–18 show the graphical results of the numerical analyses in the form of topographical maps for the PEEK/BG sample material at the pressure 0.5 MPa and the simulation of the rider-plate tribological friction

**Fig. 6** Three-dimensional (3D) CAD models of the RS2007 tester. **a** rider-plate (the direction of the motion), **b** tribological friction couple (the applied force)

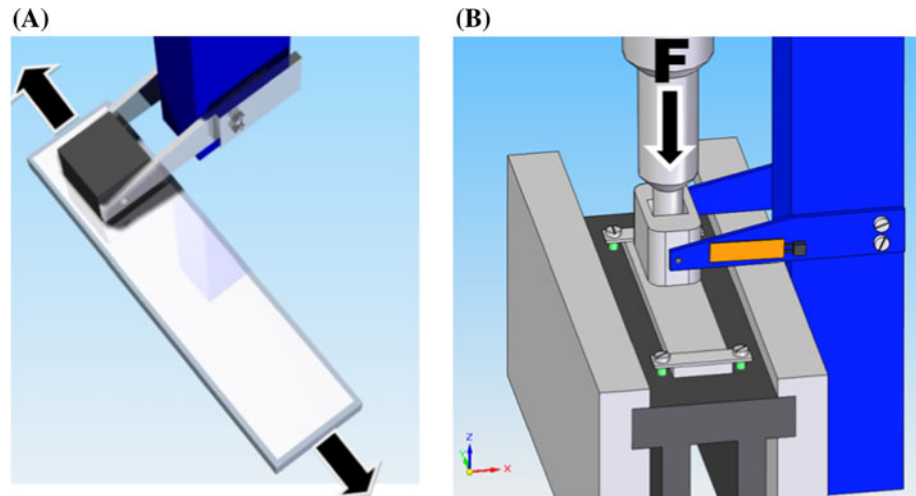


**Table 1** Material properties entered to Autodesk multiphysics simulations

Material properties	EN AW-5251	Al <sub>2</sub> O <sub>3</sub>	TG15	TGK20/5	TMP12	PEEK/BG
Mass density (kg/m <sup>3</sup> )	2,680	3,960	2,150	2,110	2,260	1,447
Modulus of elasticity (MPa)	69,300	370,000	460	460	490	8,730
Poisson's ratio	0.36	0.22	0.46	0.46	0.46	0.4
Friction coefficient between layer and material	–	–	0.21	0.25	0.35	0.19

couple. Other results for all tested materials are compiled in Table 2. The results obtained are mainly the consequence of the reference to the first principal stress. Every colour in the presented topographic maps of stresses corresponds to a specific level range of stresses occurring on the surface. The results of von Mises analyses for selected boundary conditions indicate the presence of the highest stresses for the specific tribological system examined in areas of contact between the rider (PEEK/BG) and the Al<sub>2</sub>O<sub>3</sub> layer formed on the plate (Fig. 7). The analysis of Tresca maximum stresses yielded essentially identical visual results, while the values of stresses changed slightly (Fig. 8). Maximum von Mises stresses in the block, regardless of the material used, were found at the bottom in the tribological contact place of the block and the layer (Fig. 9). Motion and pressure on the sample induced stresses that increased in the direction of the motion of the block in the ceramic coating separating the sample from the counter-sample (Fig. 10). The occurrence of large stress fields in the coating was observed, both from the front and from the back of the place where the sample was applied. The results of strains for the same system together with boundary conditions are shown in Fig. 11. Maximum strains in the block which induced friction forces and abrasion of the surface of the block in technically dry friction conditions occurred at the place of contact between the surface of the block and the oxide layer in the direction

**Table 2** The results of analyses for variable boundary conditions for maximum values

Material	Force (MPa)	Stress (MPa)	Strain	Coating strain	Displacement (mm)
PEEK/BG	0.25	2.7389	0.000239	8.30E–06	0.00094166
	0.5	3.7411	0.000318	1.13E–05	0.001166
	1	5.7549	0.000478	1.74E–05	0.00168
TG15	0.25	3.0273	0.00456	9.16E–06	0.0159
	0.5	5.2610	0.00620	1.29E–05	0.0165
	1	8.0768	0.01205	1.68E–05	0.0289
TGK20/5	0.25	3.8699	0.00588	1.24E–05	0.0170
	0.5	5.2610	0.01014	1.70E–05	0.0231
	1	8.7739	0.01850	2.60E–05	0.0472
TMP12	0.25	4.2498	0.005377	1.29E–05	0.01744
	0.5	6.7044	0.00990	2.03E–05	0.0307
	1	11.6837	0.01668	3.53E–05	0.0514

of the motion of the block (Fig. 12). The highest energy absorbed by the component due to loads in the sample was generated in the corners of the block (Fig. 13). Topographic maps of the distribution of strains in the thin layer obtained on the aluminium alloys with the marked spot where the maximum strains occurred are shown in Fig. 14. Magnification of the image of maximum strains and dislocations indicates the formation of macromechanical tribological mechanisms which changed the shape of the



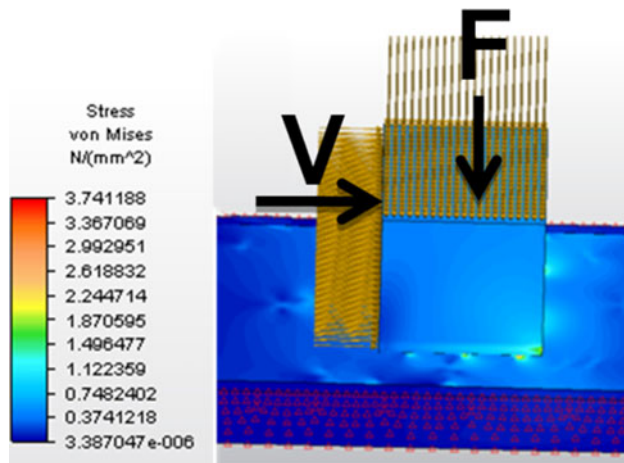


**Fig. 7** Boundary conditions and the results of von Mises stress analysis

surface and induced local strains (Fig. 15). The value of maximum dislocations in the layer with no magnification is shown in Fig. 16. Applying force causing the motion of the rider caused its slight shifting shown in enlargement in Fig. 17. The conducted dynamic analysis of stresses (Fig. 18) also confirmed the non-uniformity of the sliding film formation. It is evident that the value of the stress was not completely uniform, which may explain the phenomenon of non-uniform sliding film formation during stand tests (Fig. 19).

The conducted numerical analysis using the FEM in the Autodesk Simulation programme for variable pressures and materials yielded results regarding maximum stresses, strains and dislocations in the sample and the oxide layer (Table 2).

Maximum stresses for the examined tribological couple were observed in the ceramic layer. In couples with variable sample materials these average values for these couples were: PEEK/BG—4.08 MPa, TG15—5.46 MPa, TGK20/5—5.97 MPa and TMP12—7.55 MPa. The maximum stress for TMP12 was almost twofold higher than that for PEEK/BG. The highest average value occurred in the sample material TMP12 (0.011506667); the lowest average

**Fig. 8** Values of Tresca maximum stresses in the rider-plate system

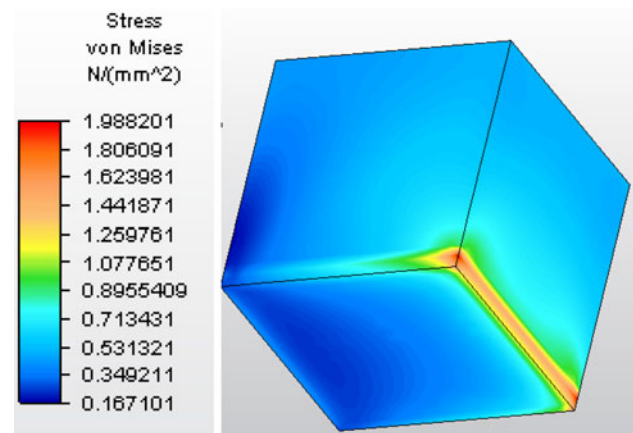
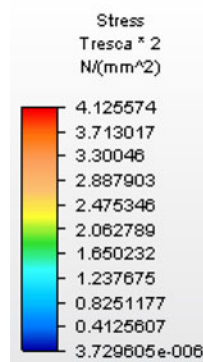


**Fig. 9** von Mises stress in rider

value occurred in PEEK/BG (0.000345). The values of average maximum strains in the layer during interaction with examined materials amounted to: PEEK/BG—0.0000123, TG15—0.0000130, TGK20/5—0.0000184, and TMP12—0.0000228. In accordance with Hook's law, strains increased with increases in stress. Maximum dislocations in the examined sample-counter-sample friction couple occurred in the rider. The lowest value obtained was for the PEEK/BG material (average 0.00126) and the highest was for TMP12 (average 0.03318). Analysis of the results revealed their correlation with the stand tests (Fig. 20) conducted on a real tester for a friction distance of 70 km. The test on the tester RS2007 was conducted in technical dry friction conditions. The unit pressure was 0.25 MPa, with the average slide speed of 1 m/s using a reciprocating motion. To confirm the correctness of the results the tribological tests were repeated four times. The length of the test was set to 70 km because at this stage wearing-in of the mating pair takes place and subsequent mating—the relation of friction and wear—has a linear character. The friction coefficient was also measured (Fig. 21). One can assume that growing stress (Fig. 22) and strain (Fig. 23) values lead to the increase in wear of the sample material and the oxide layer.

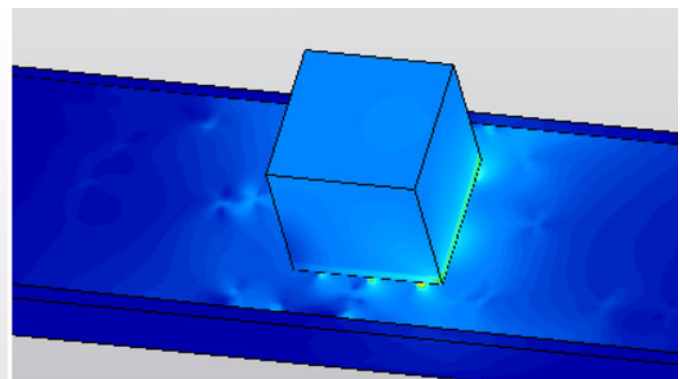


**Fig. 10** A topographic map of the distribution of von Mises stresses in the oxide layer

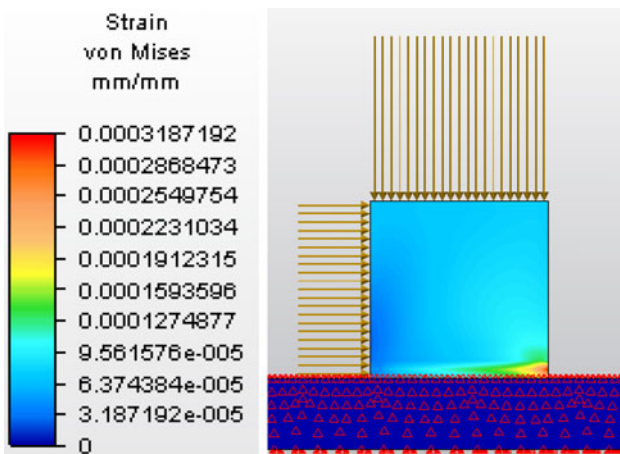
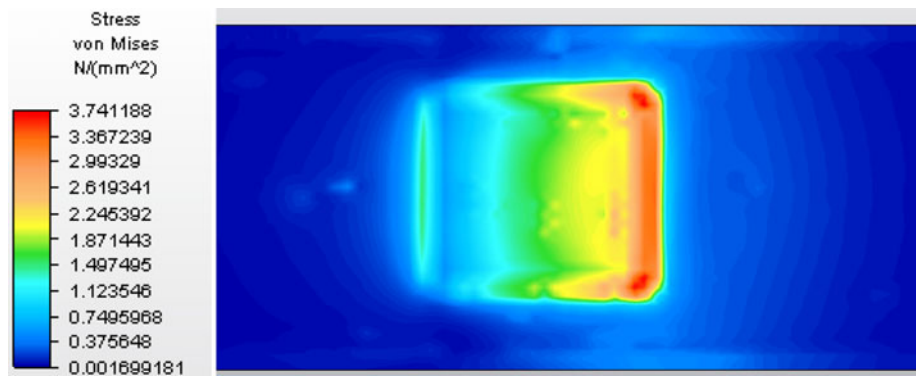


**Fig. 11** von Mises strains in the rider-plate couple

The increase of stresses affecting the samples causes the increase of strains. This value is linear, from which it can be concluded that these strains are elastic. The test results show that the tribological properties in the tested friction couple depend on the properties of sample and counter-sample material and the value of the surface pressure of the friction coefficient.

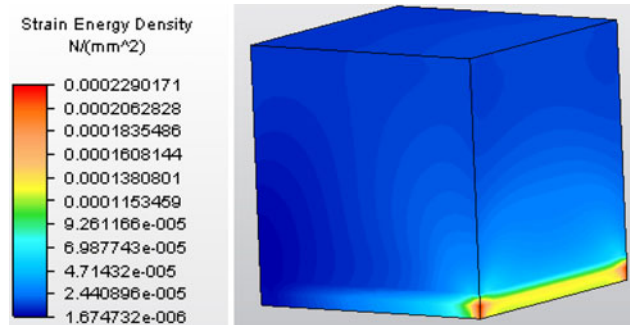


**Fig. 13** Strains in energy density in the rider

#### 4 Conclusions

The combination of stand tests and computer technology allowed us to create a 3D model of the oxide layer. The ceramic layer was obtained on the EN AW-5251 aluminium alloy in a three-component SAS electrolyte at a temperature of 298.15 K, a current density of 3 A/dm<sup>2</sup> and an oxidation time of 60 min. Following the application of a computer image analysis and the preparation of binary images, we measured the size of nonporous nanofibres and the thickness of the nanofibres on scanning microscopic images, which made it possible to model a body

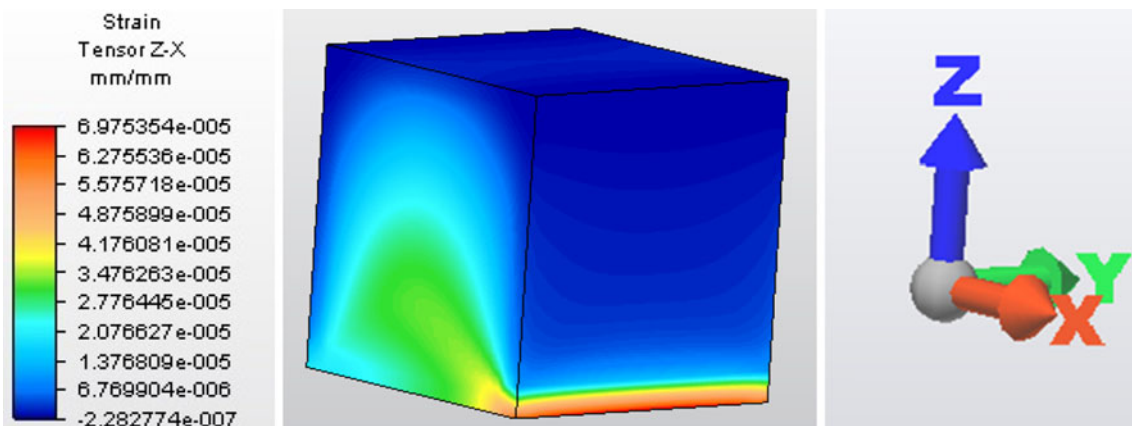


**Fig. 12** The distribution of strains in the Z–X direction in the block

**Fig. 14** Topographic maps of the distribution of strains in the thin layer obtained on the aluminium alloy

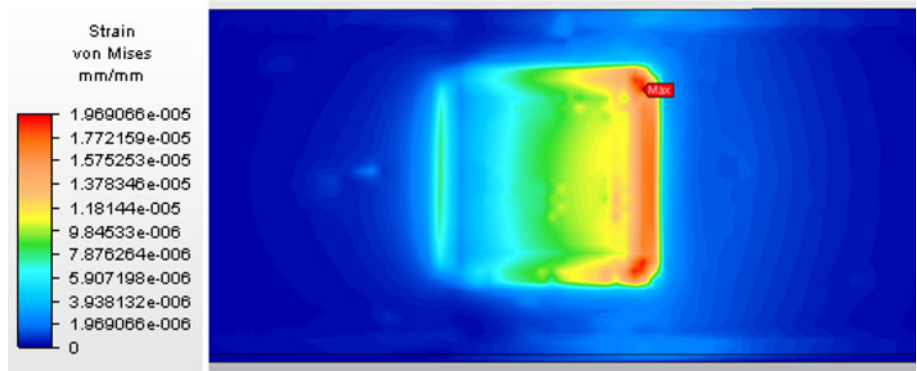
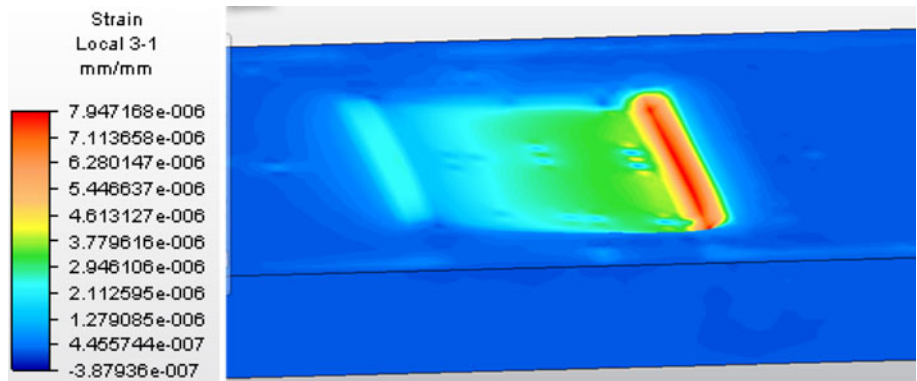
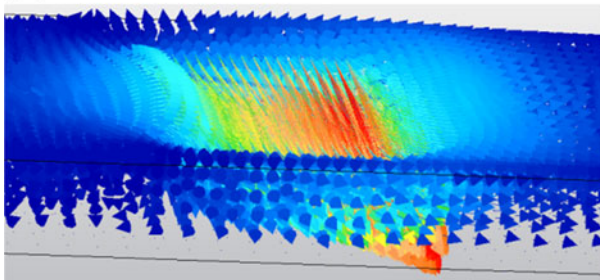


**Fig. 15** Maximum local strains in oxide layer



**(A)**



**(B)**

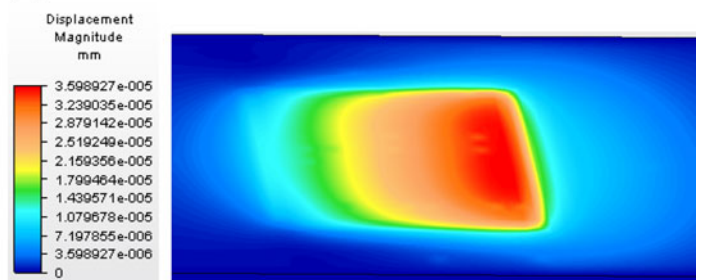


**Fig. 16** Displacement in coating. **a** Magnification vector plot, **b** smooth magnitude

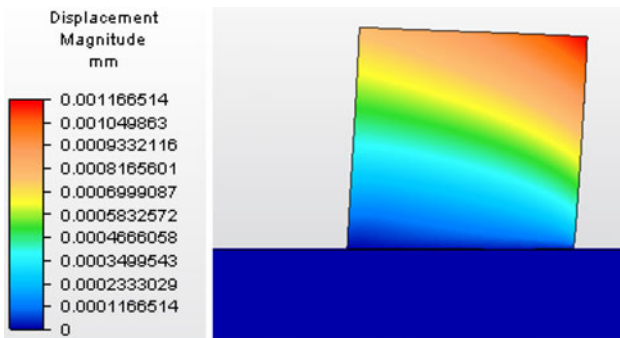


**Fig. 17** Magnified displacement magnitude in the tribological couple

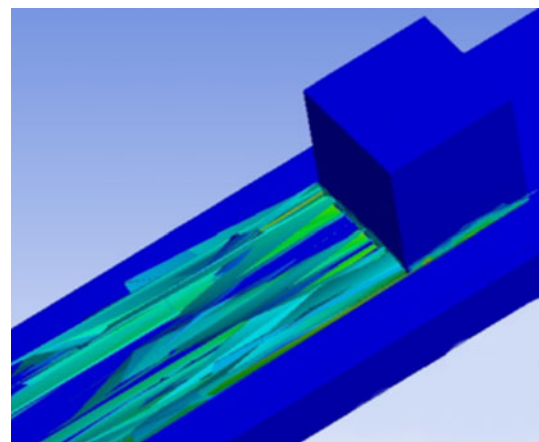


**Fig. 18** The distribution of stresses obtained from the modelling of the slide of the rider on the plate for dynamic analysis in reciprocating motion



**Fig. 19** Oxide coating representing the counter-specimens after the tribological tests [19]

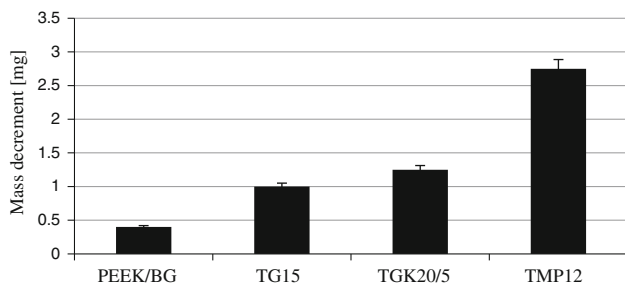


**Fig. 20** The results of stand tests of the wear of composites interacting with the oxide layer with the use of various materials for a friction distance of 35 km

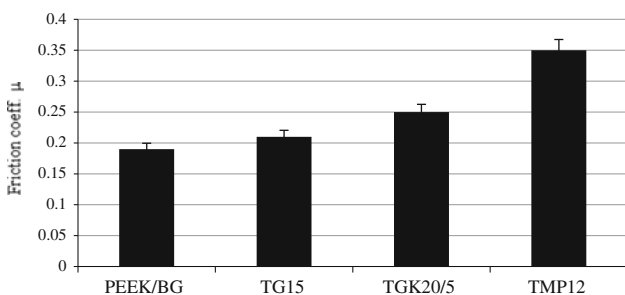


**Fig. 21** The results of the friction coefficient

representing the Al<sub>2</sub>O<sub>3</sub> layer and its morphology in the Solid Edge computer design support programme.

The body representing the actual rider-plate friction couple was imported from the CAD programme to the

CAE environment where numerical calculations were made. The use of computer simulation in the Autodesk Simulation programme to examine tribological phenomena allowed the occurrence of stresses, strains and dislocations in the sample and counter-sample material with the obtained Al<sub>2</sub>O<sub>3</sub> to be illustrated. The tests were conducted in technically dry friction conditions at variable pressures and with different materials. Strains in the surface and visible mechanical properties are the results of the action of motion and pressure on the block which interacts directly with the oxide layer. The results of numerical tests show that tribological properties depended on the properties of materials used in the test and on the value of the surface pressure of the friction coefficient. In accordance with Hook’s law, the increase of stresses caused the increase of strains. In the case examined here, there was a linear dependence between stresses and strains, which means that we are dealing with plastic strains. On the basis of the analysis of stress fields results in the oxide layer it can be concluded that they are induced by:

1. Friction force—friction between the moving sample and the oxide layer induces compression stresses caused by the push force and tensional stress.
2. Changes in geometry—plastic strains induced by compression and tension occur in the layer. They are consistent with macromechanical tribological mechanisms. For example, the inclination of the block and deflection of the layer can be observed.
3. Residual stresses—these are particularly common in thin ceramic coatings due to the deposition process and they may contain high-value compression stresses.

Stresses in the ceramic layer increased in the direction of the motion, although the occurrence of large stress fields was visible both from the front and from the back of the place where the block was applied. Maximum strains in the block occurred at the place of contact between the surface of the block and the oxide layer. The highest energy

**Fig. 22** Maximum stresses in the oxide layer

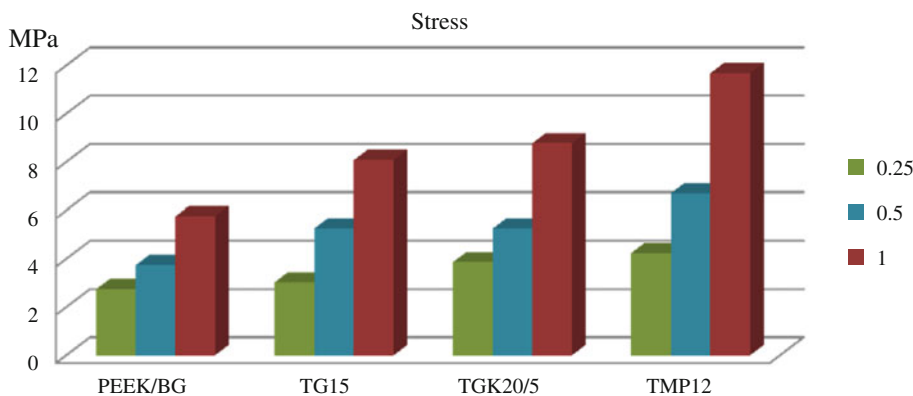
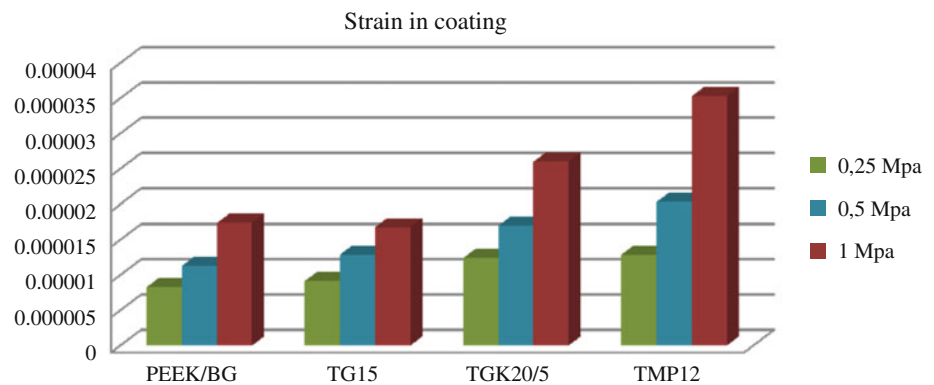


**Fig. 23** Maximum strains in the oxide layer



absorbed by the component due to loads in the sample was generated in the corners of the block. The value of maximum strains in the  $\text{Al}_2\text{O}_3$  layer was not distributed uniformly, which may explain the phenomenon of non-uniform spread of a sliding film formed during stand tests.

**Open Access** This article is distributed under the terms of the Creative Commons Attribution License which permits any use, distribution, and reproduction in any medium, provided the original author(s) and the source are credited.

## References

- Bhushan, B.: Introduction of tribology. Wiley, New York (2002)
- Sobiecki, J., Tomassi, P.: The production of laminar composite Al– $\text{Al}_2\text{O}_3$ . *Composites* **6**, 20–25 (2006)
- Woydt, M., Skopp, A., Dörfel, I., Witke, K.: Wear engineering oxides/antiwear oxides. *Tribol. Trans.* **42**, 21–31 (1999)
- Pytko, S., Szczerek, M.: Forecast of development directions of tribological research. *Maintenance Probl.* **1**, 99–107 (1998)
- Kurtyka, P., Wierzbiński, S., Faryna, M.: Selected mechanical properties of composites based on aluminium alloys reinforced  $\text{Al}_2\text{O}_3$  particles. *Composites* **4**, 185–190 (2002)
- Olszówka-Myalska, A.: Influence of alumina particles preparation with nickel on aluminium matrix composite properties. *Composites* **4**, 199–203 (2002)
- Gabe, D.: Hard anodizing—what do we mean by hard? *Met. Finish.* **100**, 52–58 (2002)
- Patermarkis, G., Moussoutzanis, K.: Electrochemical kinetic study on the growth of porous anodic oxide films on aluminium. *Electrochem. Acta* **40**, 699–708 (1995)
- Csokan, P.: *Advances in Corrosion Science and Technology*, vol. 7, pp. 239–356. Plenum Press, New York and London (1980)
- Keller, F., Hunter, M., Robinson, D.: Structural features of oxide coatings on aluminium. *J. Electrochem. Soc.* **100**, 411–419 (1953)
- Lee, W., Schwim, K., Steinhartm, M., Pippel, E., Scholz, R., Gosele, U.: Structural engineering of nanoporous anodic aluminium oxide by pulse anodisation of aluminium. *Nat. Nanotechnol.* **3**, 234–239 (2008)
- Lia, D., Jianga, C., Rena, X., Longb, M., Jianga, J.: Fabrication of porous anodic alumina membranes with ultrathick barrier layer. *Mater. Lett.* **62**, 3228–3231 (2008)
- Sulka, G.D.: Highly ordered anodic porous alumina formation by self-organised anodising and template-assisted fabrication of nanostructured materials. In: Eftekhari, A. (ed.) *Nanostructured materials in electrochemistry*, pp. 1–116. Wiley-VCH, Weinheim (2008)
- Zaraska, L., Stępniewski, W., Ciepela, E., Sulka, G.: The effect of anodizing temperature on structural features and hexagonal arrangement of nanopores in alumina synthesized by two-step anodizing in oxalic acid. *Thin Solid Films* **534**, 155–161 (2013)
- Skoneczny, W.: Analysis of morphology and microstructure of  $\text{Al}_2\text{O}_3$  layers. *Mater. Sci.* **46**, 276–281 (2010)
- Eftekhari, A.: *Nanostructured materials in electrochemistry*. Wiley-VCH, Weinheim (2008)
- Gumowska, W., Dobosz, I., Uhlemann, M., Koza, J.:  $\text{Al}_2\text{O}_3$ –Co and  $\text{Al}_2\text{O}_3$ –Fe composites obtained by the electrochemical method. *Arch. Metall. Mater.* **54**, 1119–1133 (2009)
- Fratila-Apachitei, L., Terry, H., Skeldon, P., Thompson, G., Katgerman, L.: Substrate microstructure on the growth of anodic oxide layers. *Electrochem. Acta* **49**, 1127–1140 (2004)
- Kmita, T., Skoneczny, W.: Increase of operational durability of a plastic material-oxide coating couple as a result of the application of a pulsed anodizing process. *Maintenance Reliab.* **1**, 77–82 (2010)
- Kubica, M., Skoneczny, W., Służalek, G.: Computer image analysis and modeling of nanoceramic oxide layer. *Mechanik* **7**, 469–476 (2011)
- Tichy, J.: Modeling of thin film lubrication. *Tribol. Trans.* **38**, 108–118 (1995)
- [http://wikihelp.autodesk.com/Autodesk\\_Simulation/enu/2012/Help/0531-Results531/0533-Results\\_533/0535-Results\\_535/0536-Linear\\_R536](http://wikihelp.autodesk.com/Autodesk_Simulation/enu/2012/Help/0531-Results531/0533-Results_533/0535-Results_535/0536-Linear_R536) (9 Jan 2011)
- Holmberg, K.: The basic material parameters that control friction and wear of coated surfaces under sliding. *Tribol. Finn. J. Tribol.* **19**, 3–18 (2000)
- Rickerby, D., Matthews, A.: *Advanced surface coatings: a handbook of surface engineering*. Blackie, Glasgow (1991)
- Oliver, W., Pharr, G.: An improved technique for determining hardness and elastic modulus using load and displacement sensing indentation experiments. *J. Mater. Res.* **7**, 1564–1583 (1992)
- Ye, N., Komvopoulos, K.: Indentation analysis of elastic-plastic homogeneous and layered media: criteria for determining the real material hardness. *J. Tribol.* **125**, 52–59 (2003)
- Raveeh, A., Tsameret, Z., Grossman, E.: Surface characterization of thin layers of aluminium oxide. *Surf. Coat. Technol.* **88**, 103 (1996)
- Jeurgens, L., Sloof, W., Tichelaar, F., Mittemeijer, E.: Growth kinetics and mechanisms of aluminium-oxide films formed by thermal oxidation of aluminium. *J. Appl. Phys.* **92**, 81–84 (2002)
- Miyamoto, Y., Kaysser, W., Rabin, B., Kawasaki, A., Ford, R.: *Functionally graded materials: design, processing, and applications*. Kluwer Academic Publishers, Boston (1999)

30. Hsing-Hsiang, S., Shiang-Lin, T.: Study of anodic oxidation of aluminium in mixed acid using a pulsed current. *Surf. Coat. Technol.* **124**, 278–285 (2000)
31. Kmita, T., Duda, P., Kaptacz, S., Skoneczny, W.: The influence of the radius of the rubbing contact tract on the wear of the PEEK/BG plastic mating with the oxide coating. *Tribologia* **212**, 251–260 (2007)
32. Burakowski, T., Wierzchom, T.: *Inżynieria powierzchni metali: podstawy, urządzenia, technologie*. WNT, Warszawa (1995)
33. Skoneczny, W., Tokarz, A.: Mechanism of destructive changes in oxide-covered surfaces caused by friction. *Wear* **169**, 209–214 (1993)
34. Kmita, T., Skoneczny, W.: Gradient layers on aluminium alloys created electrolytically. *Chem. Process Eng.* **26**, 735–744 (2005)
35. Skoneczny, W.: Analysis of the friction parameters of the oxide covers slide against the plastic TG 15. *Tribologia* **1**, 69–79 (1998)
36. Skoneczny, W.: *Kształowanie właściwości warstw wierzchnich aluminium I jego stopów metodą anodowania*. Politechnika Łódzka, Bielsko-Biała (2001)
37. Fei, L., Feng-yuan, Y., Lai-gui, Y., Wei-min, L.: The tribological behaviors of copper-coated graphite filled PTFE composites. *Wear* **237**, 33–38 (2000)
38. Quadrini, F., Squeo, E.: Injection molding of bushes made of tribological PEEK composites, *eXPRESS. Polym. Lett.* **12**, 817–823 (2007)
39. Harsha, A., Tewari, U.: Tribo performance of polyaryletherketone composites. *Polym. Test.* **21**, 697–709 (2002)
40. Harsha, A., Tewari, U., Venkatraman, B.: Solid particle erosion behaviour of various polyaryletherketone composites. *Wear* **254**, 693–712 (2003)
41. Zhang, Z., Breidt, C., Chang, L., Friedrich, K.: Wear of PEEK composites related to their mechanical performances. *Tribol. Int.* **37**, 271–277 (2004)
42. Jacobs, O., Jaskulka, R., Yan, C., Wu, W.: On the effect of counterface material and aqueous environment on the sliding wear of various PEEK compounds. *Tribol. Lett.* **18**, 359–372 (2005)